On the handling of automated vehicles: Modeling, bifurcation analysis, and experiments

Sanghoon Oh [a,*], Sergei S. Avedisov [a,b], Gábor Orosz [a,c]

[a] *Department of Mechanical Engineering, University of Michigan, Ann Arbor, MI 48109, USA*
[b] *Toyota InfoTechnology Center, Mountain View, CA 94043, USA*
[c] *Department of Civil and Environmental Engineering, University of Michigan, Ann Arbor, MI 48109, USA*

ARTICLE INFO

ABSTRACT

The dynamics of automated vehicles are studied and the existence and stability of steady state cornering maneuvers are investigated. Utilizing tools from analytical mechanics, namely the Appellian approach, vehicle models are constructed which incorporate geometrical nonlinearities and differentiate between front wheel drive (FWD) and rear wheel drive (RWD) automobiles. The dynamics of these models are studied using bifurcation analysis. Stable and unstable steady states are mapped out as a function of speed and steering angle. It is demonstrated that RWD and FWD vehicles exhibit different behavior, especially when they operate close to their handling limits. The theoretical results are verified experimentally using an automated vehicle performing safety critical maneuvers.

1. Introduction

Automated vehicles are likely to enter our roads soon and they need to satisfy more strict safety requirements compared to their human-driven counterparts (Ersal et al., 2020). For motion planning and control of automated vehicles choosing an appropriate model is important. The model must have high enough fidelity to be able to predict the motion of the vehicle accurately, while in the meantime it must be simple enough so it can be run in realtime. When focusing on the lateral and yaw motion, the so-called single track or bicycle model is often used to plan the motion of the vehicle and to track the planned trajectory by steering the vehicle (Popp and Schiehlen, 2010; Schramm et al., 2014; Rajamani, 2012; Ulsoy et al., 2012). In this paper we consider this modeling approach and show that by adding important geometric nonlinearities one can improve the predictive power of bicycle models without significantly increasing their complexity.

While in many scenarios assuming rigid wheels can be used to simplify the model (Paden et al., 2016; Várszegi et al., 2019), taking into account the deformation of the tires is important when trying to predict and control the motion of the vehicle; especially, close to its handling limits (Liu et al., 2016). One of the earliest work about the bicycle model with tires can be found in Riekert and Schunck (1940), and since then there has been a large number of publications following this approach. These models mainly differ in how the tire-road interaction is modeled. Since the lateral deformation of a tire leads to the formation of a slip angle between the direction of the wheel plane and the direction of velocity of the wheel center, the lateral force arising due to this deformation is often expressed as a function of the tire slip angle (Pacejka, 2005). Nevertheless, more precise tire models that capture the effects of the tire deformation along the contact patch have been recently proposed and analyzed (Beregi and Takács, 2019; Mi et al., 2020).

In general, the lateral force is a nonlinear function of the slip angle and this nonlinearity was taken into account in prior studies using the bicycle model. In earlier works, bifurcations of a bicycle model with nonlinear tire characteristics were investigated (Ono et al., 1998; Della Rossa et al., 2012; Farroni et al., 2013) and steering controllers were designed in order to maintain lateral stability (Voser et al., 2010). More recent studies about lateral stabilization and operating vehicles at their handling limits relied on boundaries in state space related to the peak lateral tire forces (Hwan Jeon et al., 2013; Erlien et al., 2013). However, the actual region of attraction of steady states may differ from these boundaries depending on the steering angle and the drive type. Moreover, mapping out the detailed state space picture may allow one to design high-performance controllers. Indeed, many recent research efforts in automated vehicle control is related to driving vehicles at their handling limits (Li et al., 2020; Berntorp et al., 2020; Wurts et al., 2020; Lu et al., 2021), including the control of unstable motions like drifting (Velenis et al., 2011; Goh et al., 2020), in order to improve the vehicle's agility. However, existing models do not differentiate between

---

* Corresponding author.
  E-mail address: osh@umich.edu (S. Oh).

Table 1
Parameters of a 2016 KIA Soul automobile used in this paper.

	Parameter name	Value	Unit
m	Vehicle mass	1110	kg
J_G	Vehicle mass moment of inertia	1343	kg m^2
c	Vehicle center of mass position	1.03	m
d	Vehicle center of mass position	1.54	m
$l = c + d$	Wheelbase	2.57	m
k	Distributed tire stiffness	4×10^6	N/m^2
a	Half contact length	0.1	m
$C = 2ka^2$	Cornering stiffness	8×10^4	N/rad
μ	Sliding friction coefficient	0.6	
μ_0	Static friction coefficient	0.9	

Fig. 1. (a) Bicycle model with geometric, kinematics and dynamics quantities indicated. (b) Nonlinear tire characteristics for brush model (blue) and magic formula (green). The location of peak force $\alpha_{\rm pk}$, the beginning of the sliding region $\alpha_{\rm sl}$, the cornering stiffness $C = \frac{{\rm d}F}{{\rm d}\alpha}(0)$ and the saturation force μF_z are indicated. (For interpretation of the references to color in this figure legend, the reader is referred to the web version of this article.)

drive types, which provide a fundamental limitation for the predictive power of the models as well as for the performance of the designed controllers. This limitation is particularly important to overcome if one wishes to exploit the opportunities brought by the integration of vehicle automation and electrification (Zhang et al., 2018).

To answer this challenge, in this study we utilize the Appellian approach (Gantmacher, 1975; De Sapio, 2017) and construct nonlinear bicycle models which, in addition to the tire nonlinearities, incorporate geometric nonlinearities. We demonstrate that these models are able to bring out the qualitative differences between rear wheel drive (RWD) and front wheel drive (FWD) automobiles. We use bifurcation analysis to investigate the steady state cornering while varying the steering angle and the speed of the vehicle. The bifurcation diagrams and state space pictures reveal stable and unstable turning motions and the regions of attractions for the former ones. These diagrams allow us to explore the similarities and differences between the behavior of RWD and FWD vehicles. The theoretical results are validated with a help of an automated vehicle driven up to its handling limits. We also point out specific unstable motions which, if stabilized by appropriate control design, can significantly enhance the maneuverability of automated vehicles.
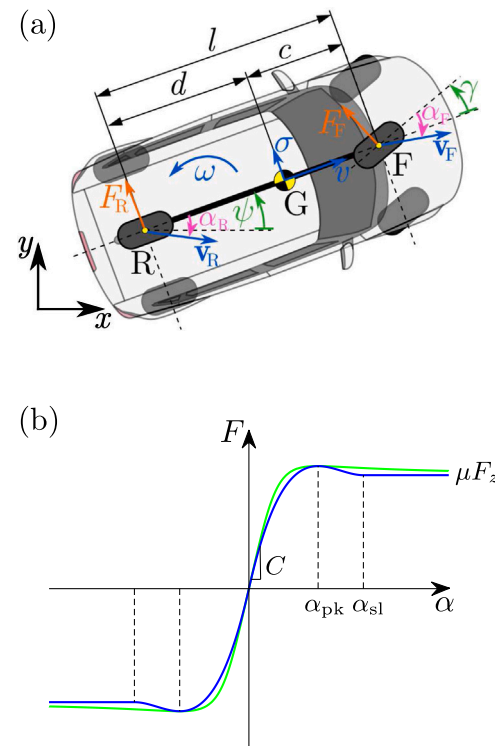
The paper is organized as follows. In Section 2 we describe the governing equations and the cornering characteristics of a so-called traditional model with tire nonlinearity. In Section 3 we provide the derivation of the equations of motion of the proposed nonlinear models for RWD and FWD vehicles using the Appellian approach and show that these models simplify to the traditional model for small steering angles. Section 4 contains the analysis of steady state cornering for different models using numerical continuation. In Section 5 we discuss the experimental results that validate the FWD model. In Section 6 we conclude our work and propose future research directions.

2. Traditional bicycle model

In this section we describe a version of the bicycle model that has been used in the literature. We refer to this as the traditional bicycle model in the remaining of the paper. While discussing this model we also introduce some basic notations and terminology related to the steady state cornering. Finally, we point out some of the shortcomings of this traditional model.

Fig. 1(a) shows the schematic diagram of a bicycle model for an automobile with front wheel steering. In this model the front wheels are united as one wheel and the rear wheels are also united as one wheel. The mass of the vehicle is m, its mass moment of inertia about the center of mass G is denoted by J_G, the wheel base in given by l, the distance between the center of the front axle F and the center of mass G is given by c while the distance between the center of the rear axle R and the center of mass G is given by d. Indeed we have $l = c + d$. The parameters used in this paper are listed in Table 1.

The vehicle can be described by three configuration coordinates and these are typically chosen to be the position of the center of mass (x_G, y_G) and the yaw angle ψ. The velocity state is typically given

by the angular velocity ω called the yaw rate, and by the velocity components of the center of mass G resolved in the frame fixed to the vehicle's body, referred to as longitudinal velocity v and lateral velocity σ; see Fig. 1(a). The kinematic relationships between the derivatives of the configuration coordinates and the velocity components can be expressed by

$$\dot{x}_G = v \cos\psi - \sigma \sin\psi,$$
$$\dot{y}_G = v \sin\psi + \sigma \cos\psi, \tag{1}$$
$$\dot{\psi} = \omega.$$

Also, we assume that the steering angle γ can be assigned by the controller of the automated vehicle which is the input in the dynamical systems constructed below.

The rest of the modeling effort shall go into deriving differential equations for the longitudinal velocity v, the lateral velocity σ, and the yaw rate ω. Due to the elasticity of the rear tire, the velocity $\mathbf{v}_R$ of the wheel center point R is not aligned with the rear wheel plane but it forms the slip angle α_R. Similarly, for the front wheel, the velocity $\mathbf{v}_F$ of the wheel center point F is not aligned with the front wheel plane but it forms the slip angle α_F. The lateral tire deformations lead to the lateral forces F_R and F_F that are indicated in Fig. 1(a).

By approximating the deformation along the contact patch with a straight line, the lateral force can be expressed as a function of the slip angle as given in the Appendix and visualized by the blue curve in Fig. 1(b). This is often referred to as the brush model. The slip angle $\alpha_{\rm pk}$ corresponds to the peak value of the lateral force while $\alpha_{\rm sl}$ marks the limit of complete sliding. When the slip angle exceeds the latter value, the lateral force saturates at μF_z, as indicated in the figure, where F_z is the normal force and μ is the sliding friction (as opposed to the static friction that is denoted by μ_0). Finally, the derivative $C = \frac{{\rm d}F}{{\rm d}\alpha}(0)$ is also highlighted. This is referred to as the cornering stiffness and for the

brush model it can be calculated as $C = 2ka^2$ where k denotes the distributed tire stiffness and a is the half contact length; see Table 1 for the numerical values used in the paper.

For comparison, an empirical model, called the magic formula (Pacejka, 2005), is also shown in Fig. 1(b) by the green curve; see corresponding formula in the Appendix. The four independent parameters appearing in the nonlinear tire characteristics are matched for the brush model and the magic formula by matching the location and the value of the peak, the saturating value of the lateral force, and the cornering stiffness. In this paper we consider the brush model but the results shall look very similar for the magic formula. We remark that the tire deformations also lead to aligning moments but those have typically small effects in scenarios investigated in our paper, and thus, they are neglected. Finally, we mention that the longitudinal slip is neglected in this paper in order keep the complexity of the model low. We found that the longitudinal forces required to keep the longitudinal velocity constant are typically much smaller than the peak lateral force. They may reach around 10%–15% of the peak lateral force in a small velocity range, where one may use higher degree of freedom models incorporating both lateral and longitudinal tire deformations.

2.1. Equations of motion

When focusing on handling it is often considered that the longitudinal velocity is constant, i.e., $v(t) \equiv v^*$, which can be ensured by applying the appropriate driving force. Moreover, it is often assumed that the steering angle and the slip angles are small and the geometrical nonlinearities can be neglected, which lead to

$$
\alpha_R = -\frac{\sigma - d\,\omega}{v^*},
$$
$$
\alpha_F = \gamma - \frac{\sigma + c\,\omega}{v^*},
$$
(2)

cf. (29) and (37) for the nonlinear versions developed further below. Similarly, one may neglect the geometrical nonlinearities when calculating the force components normal to the body and obtain

$$
\dot{\sigma} = \frac{F_R(\alpha_R) + F_F(\alpha_F)}{m} - v^*\omega,
$$
$$
\dot{\omega} = \frac{-d\,F_R(\alpha_R) + c\,F_F(\alpha_F)}{J_G},
$$
(3)

that are the Newton–Euler equations for the lateral and rotational motions, respectively; cf. (28) and (36) for the nonlinear versions developed further below. Here F_R and F_F denote lateral tire forces and these depend on the rear and front slip angles α_R and α_F as shown in Fig. 1, and in turn depend on the state variables σ and ω and the input γ according to (2). In summary, (1), (2), (3) provide us with five nonlinear differential equations for the state variables $x_G, y_G, \psi, \sigma, \omega$ with input γ. Notice that these equations are not fully coupled: one may first solve (2), (3) to obtain velocities σ, ω, and then solve (1) to obtain the configuration coordinates x_G, y_G, ψ.

In order to further simplify the matter, Eqs. (2), (3) are often linearized around the rectilinear motion yielding

$$
\begin{bmatrix} \dot{\sigma} \\ \dot{\omega} \end{bmatrix} = \begin{bmatrix} -\dfrac{C_R + C_F}{mv^*} & \dfrac{d\,C_R - c\,C_F}{mv^*} - v^* \\ \dfrac{d\,C_R - c\,C_F}{J_G v^*} & -\dfrac{d^2 C_R + c^2 C_F}{J_G v^*} \end{bmatrix} \begin{bmatrix} \sigma \\ \omega \end{bmatrix} + \begin{bmatrix} \dfrac{C_F}{m} \\ \dfrac{c\,C_F}{J_G} \end{bmatrix} \gamma
$$
(4)

where $C_R = \frac{\partial F_R}{\partial \alpha_R}(0)$ and $C_F = \frac{\partial F_F}{\partial \alpha_F}(0)$ denote the cornering stiffness of the rear and the front wheels, respectively. For simplicity, the so-called traditional linear model (1), (4) is often used instead of the traditional nonlinear model (1), (2), (3). However, due to the linear tire characteristics the former model is only valid far from the handling limits, i.e., in the domain $\alpha \ll \alpha_{pk}$ in Fig. 1(b).

2.2. Steady state cornering

Steady state cornering corresponds to negotiating a curve of constant radius by keeping the steering angle constant. Such a test can be conducted with an automated vehicle as explained further below in order to validate dynamical models and design controllers.

When substituting $\sigma(t) \equiv \sigma^*, \omega(t) \equiv \omega^*, \gamma(t) \equiv \gamma^*$ into (2), (3) one may obtain

$$
\alpha_R^* = -\frac{\sigma^* - d\,\omega^*}{v^*},
$$
$$
\alpha_F^* = \gamma^* - \frac{\sigma^* + c\,\omega^*}{v^*},
$$
$$
0 = F_R(\alpha_R^*) + F_F(\alpha_F^*) - mv^*\omega^*,
$$
$$
0 = -d\,F_R(\alpha_R^*) + c\,F_F(\alpha_F^*).
$$
(5)

These can be solved for the state variables σ^*, ω^* and the slip angles α_R^*, α_F^* while taking into account the nonlinear tire force characteristics (41), (42) (or alternatively (46)). Due to these nonlinearities the solutions can typically be found numerically (as detailed further below).

According to (1) the corresponding configuration coordinates read

$$
x_G^*(t) = \frac{v^*}{\omega^*}\sin(\omega^* t + \psi_0) + \frac{\sigma^*}{\omega^*}\cos(\omega^* t + \psi_0) + x_0,
$$
$$
y_G^*(t) = -\frac{v^*}{\omega^*}\cos(\omega^* t + \psi_0) + \frac{\sigma^*}{\omega^*}\sin(\omega^* t + \psi_0) + y_0,
$$
$$
\psi^*(t) = \omega^* t + \psi_0,
$$
(6)

where the constants x_0, y_0, ψ_0 are obtained from the initial conditions. The radius of the circular arc ran by the center of mass G can be calculated as

$$
R_G = \sqrt{(x_G^* - x_0)^2 + (y_G^* - y_0)^2} = \frac{\sqrt{(v^*)^2 + (\sigma^*)^2}}{\omega^*}.
$$
(7)

Similarly all points of the automobile move along circular paths. For example, the corresponding radius of the rear axle center point R is given by

$$
R_R = \frac{\sqrt{(v^*)^2 + (\sigma^* - d\,\omega^*)^2}}{\omega^*}.
$$
(8)

Of particular importance is the difference $\alpha_F^* - \alpha_R^*$ whose sign determines whether the vehicles displays understeer ($\alpha_F^* - \alpha_R^* > 0$) or oversteer ($\alpha_F^* - \alpha_R^* < 0$) behavior. Most production vehicles are designed to have understeer characteristics, but, as we will demonstrate below they may exhibit oversteer behavior for specific sets of parameters and initial conditions.

For small steering angles (and correspondingly small slip angles) one may utilize the linearized Eqs. (4) instead of (2), (3), which result in

$$
\begin{bmatrix} \sigma^* \\ \omega^* \end{bmatrix} = \begin{bmatrix} C_R + C_F & -(d\,C_R - c\,C_F) + m(v^*)^2 \\ -(d\,C_R - c\,C_F) & d^2 C_R + c^2 C_F \end{bmatrix}^{-1} \begin{bmatrix} C_F v^* \\ c\,C_F v^* \end{bmatrix} \gamma^*.
$$
(9)

Substituting these into (2) one may derive

$$
\alpha_F^* - \alpha_R^* = K_{us}\frac{v^*\omega^*}{g},
$$
(10)

where the so-called understeer coefficient

$$
K_{us} = \frac{mg}{l}\left(\frac{d}{C_F} - \frac{c}{C_R}\right),
$$
(11)

determines the understeer ($K_{us} > 0$) or oversteer ($K_{us} < 0$) behavior for small slip angles.

For most production automobiles understeer characteristic is typically ensured by having the engine at the front (that results in the weight distribution $F_{z,R} < F_{z,F} \Rightarrow d > c$) and using the same type of tires at the rear and the front (that yields $C_R \approx C_F$); see, for example, the data of a 2016 KIA Soul in Table 1. For some high-end automobiles the engine is more toward the middle/rear (that results in the even weight distribution $F_{z,R} \approx F_{z,F} \Rightarrow d \approx c$).
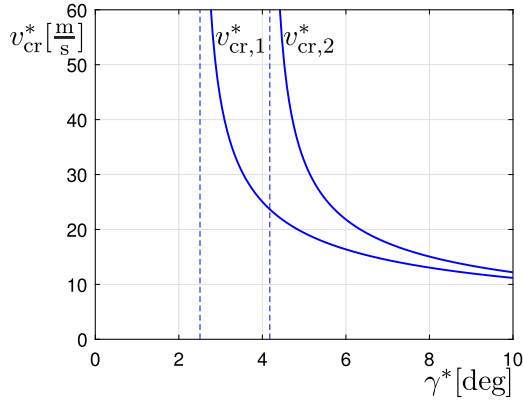
Fig. 2. The critical longitudinal velocities (13) and (15) as a function of the steering angle γ^* in case of steady state cornering.

In some special scenarios, analytical solutions of the nonlinear Eqs. (5) exist and these solutions can lead to further insight. Let us consider the case when both tires have the maximal tire force; see $\alpha = \alpha_{pk}$ in Fig. 1(b). Using the static weight distribution $F_{z,R} = mgc/l$ and $F_{z,F} = mgd/l$ in (44) we obtain

$$
\begin{aligned}
\alpha_R^* &= \arctan\left(\frac{\mu_0 mgc}{2ka^2 l}\left(1 - \frac{2\mu}{3\mu_0}\right)^{-1} \right), \\
\alpha_F^* &= \arctan\left(\frac{\mu_0 mgd}{2ka^2 l}\left(1 - \frac{2\mu}{3\mu_0}\right)^{-1} \right), \\
F_R(\alpha_R^*) &= \frac{\mu_0 mgc}{3l}\left(\frac{4}{3} - \frac{\mu}{\mu_0}\right)\left(1 - \frac{2\mu}{3\mu_0}\right)^{-2}, \\
F_F(\alpha_F^*) &= \frac{\mu_0 mgd}{3l}\left(\frac{4}{3} - \frac{\mu}{\mu_0}\right)\left(1 - \frac{2\mu}{3\mu_0}\right)^{-2}.
\end{aligned}
\tag{12}
$$

Substituting the last two equations of (12) into the third equation of (5) and substituting the first two equations of (12) into the first two equations of (5) while using the approximation $\arctan\alpha \approx \alpha$, we can calculate the critical velocity:

$$
v_{cr,1}^* \approx \sqrt{ \frac{\frac{\mu_0 lg}{3}\left(\frac{4}{3} - \frac{\mu}{\mu_0}\right)\left(1 - \frac{2\mu}{3\mu_0}\right)^{-2}}{\gamma^* - \frac{\mu_0 mg(d-c)}{2ka^2 l}\left(1 - \frac{2\mu}{3\mu_0}\right)^{-1}} },
\tag{13}
$$

which only exist for $\gamma^* > \frac{\mu_0 mg(d-c)}{2ka^2 l}\left(1 - \frac{2\mu}{3\mu_0}\right)^{-1}$. When the vehicle reaches this speed both tires provide the maximum available lateral force, that is, increasing the speed further one may expect the handling to deteriorate.

Another special scenario of interest is when the both wheel are at the sliding limit ($\alpha = \alpha_{sl}$ in Fig. 1(b)) which yields

$$
\begin{aligned}
\alpha_R^* &= \arctan\left(\frac{3\mu_0 mgc}{2ka^2 l}\right), & F_R(\alpha_R^*) &= \frac{\mu mgc}{l}, \\
\alpha_F^* &= \arctan\left(\frac{3\mu_0 mgd}{2ka^2 l}\right), & F_F(\alpha_F^*) &= \frac{\mu mgd}{l},
\end{aligned}
\tag{14}
$$

according to (41) and (43) with static weight distribution. Now, substituting the last two equations of (14) into the third equation of (5) and substituting the first two equations of (14) into the first two equations of (5), the approximation $\arctan\alpha \approx \alpha$ leads to the second critical velocity:

$$
v_{cr,2}^* \approx \sqrt{ \frac{\mu lg}{\gamma^* - \frac{3\mu_0 mg(d-c)}{2ka^2 l}} },
\tag{15}
$$

which only exists for $\gamma^* > \frac{3\mu_0 mg(d-c)}{2ka^2 l}$. When this speed is reached both tires enters full sliding and the vehicle becomes uncontrollable.

The critical velocities (13) and (15) are shown as a function of the steering angle γ^* in Fig. 2. Indeed, these velocities only exist above certain steering angles as indicated by the dashed vertical asymptotes. Also, observe that for large steering angles the two critical velocities are close to each other. We remark that there exist no analytical proof that the above special states (where both tires have maximal tire force and where both tires are at the limit of full sliding) actually exist. However, in Section 4 we will demonstrate by numerical continuation that they do in fact show up for the traditional nonlinear model (1), (2), (3) where that the analytical formulae (13) and (15) provide good approximations of the critical speeds.

Finally, we remark that apart from finding the steady states by solving (5) one may also evaluate the stability of steady state cornering by linearizing (2), (3) about the steady state. In particular, defining the perturbations $\tilde{\sigma} = \sigma - \sigma^*$, $\tilde{\omega} = \omega - \omega^*$, $\tilde{\gamma} = \gamma - \gamma^*$ one may obtain the linearized system

$$
\begin{bmatrix} \dot{\tilde{\sigma}} \\ \dot{\tilde{\omega}} \end{bmatrix} = \begin{bmatrix} -\dfrac{C_R^* + C_F^*}{mv^*} & \dfrac{d\,C_R^* - c\,C_F^*}{mv^*} - v^* \\ \dfrac{d\,C_R^* - c\,C_F^*}{J_G v^*} & -\dfrac{d^2 C_R^* + c^2 C_F^*}{J_G v^*} \end{bmatrix} \begin{bmatrix} \tilde{\sigma} \\ \tilde{\omega} \end{bmatrix} + \begin{bmatrix} \dfrac{C_F^*}{m} \\ \dfrac{c\,C_F^*}{J_G} \end{bmatrix} \tilde{\gamma}
\tag{16}
$$

where $C_R^* = \frac{\partial F_R}{\partial \alpha_R}(\alpha_R^*)$ and $C_F^* = \frac{\partial F_F}{\partial \alpha_F}(\alpha_F^*)$ are the generalized cornering stiffnesses. Note that (4) is special version of (16) where the linearization happens around the rectilinear motion.

In order to derive stability conditions for the generalized cornering stiffnesses we assume the trial solution $\tilde{\sigma} = a\,e^{st}$, $\tilde{\omega} = b\,e^{st}$, $a, b, s \in \mathbb{C}$, which results in the characteristic equation

$$
s^2 + ps + q = 0,
\tag{17}
$$

where

$$
\begin{aligned}
p &= \frac{C_R^* + C_F^*}{mv^*} + \frac{d^2 C_R^* + c^2 C_F^*}{J_G v^*}, \\
q &= \frac{l^2 C_R^* C_F^*}{m J_G (v^*)^2} + \frac{d\,C_R^* - c\,C_F^*}{J_G}.
\end{aligned}
\tag{18}
$$

The Routh–Hurwitz stability criteria $p > 0$ and $q > 0$ can be visualized in the (C_R^*, C_F^*)-plane as depicted in Fig. 3 by the green shaded domain. The boundary given by $p = 0$ (blue line) denote Hopf bifurcation: a complex conjugate pair of characteristic roots crosses the imaginary axis and oscillations arise. This is highlighted by the two panels in the right hand side that show the characteristic roots for two different parameter choices. On the other hand, the boundary given by $q = 0$ (red curve) denote fold bifurcation: a real eigenvalue crosses the imaginary axis and stability is lost in a non-oscillatory way. The two panels in the left hand side illustrate this case by showing the characteristic roots for two different parameter choices. At the intersection of the stability boundaries ($C_R^* = C_F^* = 0$) there exits a double zero characteristic root. The special states discussed above (with both tires having peak force or both tires are being at the sliding limit) are in fact correspond to this case.

While the traditional nonlinear model discussed in this section can provide insight into the dynamics of automobiles, it only incorporates the tire nonlinearities and omits the geometric nonlinearities. As will be shown below geometric nonlinearities can have significant effects on the dynamics, especially when the vehicle operates close to its handling limits. Moreover, these effects differ for front wheel drive and rear wheel drive automobiles which demand the modeling efforts discussed in the next section.

3. Bicycle models for different drive types

In this section we derive models for rear wheel drive (RWD) and front wheel drive (FWD) automobiles while taking into account the geometric nonlinearities as well as the nonlinear tire characteristics.
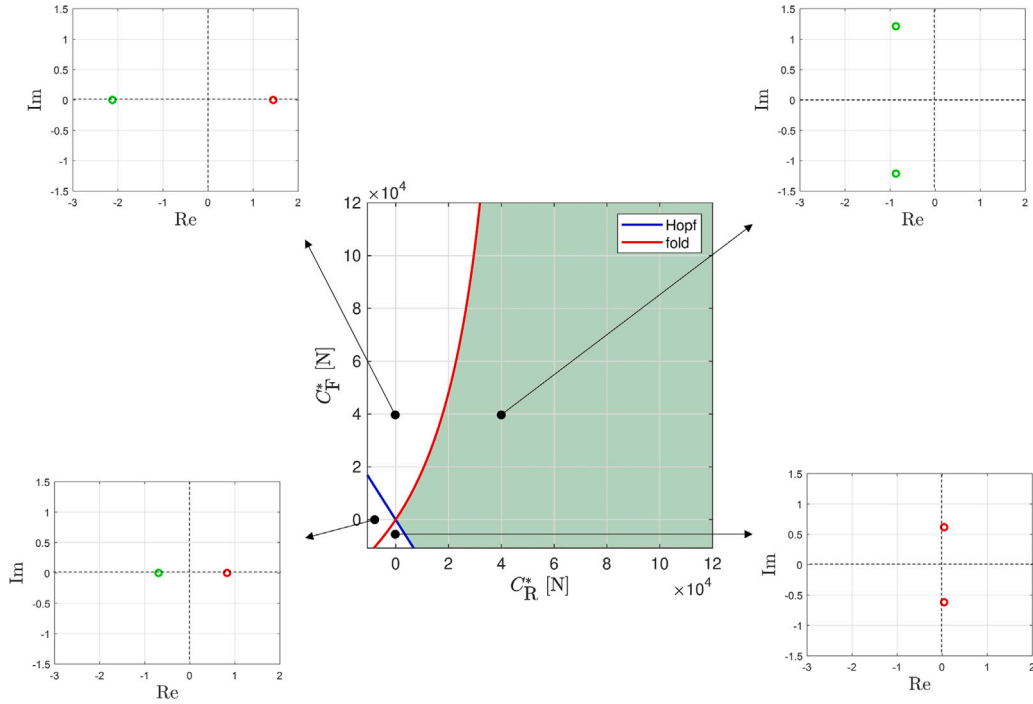
Fig. 3. Stability chart for the traditional nonlinear model on the plane of the generalized cornering stiffnesses C_R^* and C_F^*. The blue and red stability boundaries correspond to Hopf and fold bifurcations, respectively, while the stable region is shaded green. The characteristic roots are depicted in the panels on the left and the right for four different parameter sets. (For interpretation of the references to color in this figure legend, the reader is referred to the web version of this article.)

We distinguish the drive types by considering different kinematic constraints and the equations of motion are derived by using the Appellian framework. We show that both models simplify to the traditional nonlinear model, presented in the previous section, when assuming small steering and slip angles.

3.1. Rear wheel drive model

Recall Fig. 1. Again we use the three generalized coordinates (x_G, y_G, ψ) describing the position of the center of mass G and the orientation of the vehicle in the plane. We assume that the rear wheel is rolling with constant speed, that is, the longitudinal velocity of the center of the rear wheel is constant and it is denoted by v^*. This is equal to the longitudinal velocity of the center of mass G, leading to the kinematic constraint

$$\dot{x}_G \cos\psi + \dot{y}_G \sin\psi = v^*, \tag{19}$$

which is ensured by applying the appropriate driving force at the rear. Since we have 3 configuration coordinates and 1 kinematic constraint we need $3 - 1 = 2$ pseudo velocities when applying the Appellian formalism (Gantmacher, 1975; De Sapio, 2017). These are chosen to be the lateral velocity of center of mass G and the yaw rate:

$$\sigma = -\dot{x}_G \sin\psi + \dot{y}_G \cos\psi, \\ \omega = \dot{\psi}. \tag{20}$$

Eqs. (19), (20) can be solved for the generalized velocities:

$$\dot{x}_G = v^* \cos\psi - \sigma \sin\psi, \\ \dot{y}_G = v^* \sin\psi + \sigma \cos\psi, \tag{21} \\ \dot{\psi} = \omega,$$

where the first two rows give the coordinate transformation for the velocity of the center of mass G between the Earth fixed frame $(\dot{x}_G, \dot{y}_G)$ and the body fixed frame (v^*, σ).

The acceleration energy of the system can be calculated as

$$S = \frac{1}{2} m(\ddot{x}_G^2 + \ddot{y}_G^2) + \frac{1}{2} J_G \ddot{\psi}^2 \\ = \frac{1}{2} m(\dot{\sigma}^2 + 2v^* \omega \dot{\sigma}) + \frac{1}{2} J_G \dot{\omega}^2 + \cdots \tag{22}$$

where ... represent terms that do not contain the pseudo acceleration $\dot{\sigma}$ and we used the derivative of (21) when deriving the last row.

The virtual power generated by the lateral tire forces $\mathbf{F}_R$ and $\mathbf{F}_F$ can be calculated as

$$\delta P = \mathbf{F}_R \cdot \delta\mathbf{v}_R + \mathbf{F}_F \cdot \delta\mathbf{v}_F, \tag{23}$$

where $\delta\mathbf{v}_R$ and $\delta\mathbf{v}_F$ are the virtual velocities of the wheel center points R and F, respectively. In order to calculate the dot products in (23) it is convenient to resolve the velocities and forces in a frame attached to the vehicle body:

$$\mathbf{v}_R = \begin{bmatrix} v^* \\ \sigma - d\,\omega \end{bmatrix}_{\text{body}}, \qquad \mathbf{F}_R = \begin{bmatrix} 0 \\ F_R \end{bmatrix}_{\text{body}}, \\ \mathbf{v}_F = \begin{bmatrix} v^* \\ \sigma + c\,\omega \end{bmatrix}_{\text{body}}, \qquad \mathbf{F}_F = \begin{bmatrix} -F_F \sin\gamma \\ F_F \cos\gamma \end{bmatrix}_{\text{body}}. \tag{24}$$

Substituting these into (23) and using $\delta v^* = 0$ we obtain

$$\delta P = \underbrace{(F_R + F_F \cos\gamma)}_{\Pi_\sigma} \delta\sigma + \underbrace{(-d\,F_R + c\,F_F \cos\gamma)}_{\Pi_\omega} \delta\omega, \tag{25}$$

which results in the pseudo forces

$$\Pi_\sigma = F_R + F_F \cos\gamma, \\ \Pi_\omega = -d\,F_R + c\,F_F \cos\gamma. \tag{26}$$

Notice that Π_σ is the lateral component of the resultant tire force while Π_ω is the resultant moment of these forces about the center of mass G.

The Appell equations are given as

$$\frac{\partial S}{\partial \dot{\sigma}} = \Pi_\sigma, \\ \frac{\partial S}{\partial \dot{\omega}} = \Pi_\omega, \tag{27}$$

which lead to

$$\dot{\sigma} = \frac{F_R(\alpha_R) + F_F(\alpha_F) \cos\gamma}{m} - v^* \omega, \\ \dot{\omega} = \frac{-d\,F_R(\alpha_R) + c\,F_F(\alpha_F) \cos\gamma}{J_G}, \tag{28}$$

where we spelled out the that tire forces depend on the slip angles. Using the component of the velocities in (24) we obtain

$$\tan \alpha_R = -\frac{\sigma - d\,\omega}{v^*},$$
$$\tan(\alpha_F - \gamma) = -\frac{\sigma + c\,\omega}{v^*}, \tag{29}$$

where the second equation can also be rewritten as

$$\tan \alpha_F = \frac{v^* \tan \gamma - (\sigma + c\,\omega)}{v^* + (\sigma + c\,\omega)\tan \gamma}, \tag{30}$$

that is a more practical form when substituting into (41).

The equations of motion of the rear wheel drive automobile are then described by (21), (28), (29). These provide us with 5 first order differential equations which are often referred to as 2.5 degrees of freedom (DOF). Also, notice that when considering small steering angles and small slip angles, (28) simplifies to (3) and (29) simplifies to (2). That is, the rear wheel drive model simplifies to the traditional model under the small angle assumption.

We also remark that the kinematic equations for the RWD model are the same as those for the traditional model (cf. (21) and (1)). Consequently, in case of steady state cornering the radii of the center of mass R_G and the rear wheel center point R_R can be calculated by (7) and (8), respectively.

3.2. Front wheel drive model

A similar derivation can be performed for the front wheel drive vehicle where we assume that the front wheel is rolling with a constant speed. That is, the velocity component of the center of the front wheel aligned with the wheel plane is constant and it is denoted by $\hat{v}^*$. The corresponding kinematic constraint can be written as

$$\dot{x}_G \cos(\psi + \gamma) + \dot{y}_G \sin(\psi + \gamma) + c\,\dot{\psi}\sin\gamma = \hat{v}^*, \tag{31}$$

using the velocity components of the center of mass G. Again we choose the lateral velocity of center of mass G and the yaw rate as pseudo velocities; cf. (20). The system (20), (31) can be solved for the generalized velocities:

$$\dot{x}_G = \left(\frac{\hat{v}^*}{\cos\gamma} - (\sigma + c\,\omega)\tan\gamma\right)\cos\psi - \sigma\sin\psi,$$
$$\dot{y}_G = \left(\frac{\hat{v}^*}{\sin\gamma} - (\sigma + c\,\omega)\tan\gamma\right)\sin\psi + \sigma\cos\psi, \tag{32}$$
$$\dot{\psi} = \omega,$$

when $\gamma \neq \frac{\pi}{2}$, where the first two rows give the coordinate transformation for the velocity of the center of mass G between the Earth fixed frame $(\dot{x}_G, \dot{y}_G)$ and the body fixed frame $(\hat{v}^*/\cos\gamma - (\sigma + c\,\omega)\tan\gamma, \sigma)$; cf. (21).

Using the time derivative of (32) we can calculate the acceleration energy:

$$\begin{aligned}
S &= \frac{1}{2}m\left(\ddot{x}_G^2 + \ddot{y}_G^2\right) + \frac{1}{2}J_G\ddot{\psi}^2 \\
&= \frac{1}{2}\frac{m}{\cos^2\gamma}\dot{\sigma}^2 + \frac{1}{2}\left(J_G + m\,c^2\tan^2\gamma\right)\dot{\omega}^2 + m\,c\tan^2\gamma\,\dot{\sigma}\,\dot{\omega} \\
&\quad + m\left(\frac{\hat{v}^*}{\cos\gamma} - c\,\omega\tan\gamma\right)\omega\,\dot{\sigma} \\
&\quad + m\frac{\tan\gamma}{\cos^2\gamma}\left(\sigma + c\,\omega - \hat{v}^*\sin\gamma\right)\dot{\gamma}\,\dot{\sigma} \\
&\quad + m\,c\frac{\tan\gamma}{\cos^2\gamma}\left(\sigma + c\,\omega - \hat{v}^*\sin\gamma\right)\dot{\gamma}\,\dot{\omega} \\
&\quad + m\,c\,\sigma\,\omega\tan\gamma\,\dot{\omega} + \cdots,
\end{aligned} \tag{33}$$

where again ... refer to the terms without the pseudo acceleration $\dot{\sigma}$.

The velocities of the wheel center points can be expressed as

$$\mathbf{v}_R = \begin{bmatrix} \dfrac{\hat{v}^*}{\cos\gamma} - (\sigma + c\,\omega)\tan\gamma \\[2mm] \sigma - d\,\omega \end{bmatrix}_{body},$$
$$\mathbf{v}_F = \begin{bmatrix} \dfrac{\hat{v}^*}{\cos\gamma} - (\sigma + c\,\omega)\tan\gamma \\[2mm] \sigma + c\,\omega \end{bmatrix}_{body}, \tag{34}$$

in the body fixed frame while the lateral forces are still given by (24). These are used when calculating the virtual power (23) and yield the pseudo forces

$$\Pi_\sigma = F_R + \frac{F_F}{\cos\gamma},$$
$$\Pi_\omega = -d\,F_R + \frac{c\,F_F}{\cos\gamma}, \tag{35}$$

cf. (25), (26).

Then the Appell Eqs. (27) become

$$\begin{bmatrix} \dfrac{m}{\cos^2\gamma} & m\,c\,\tan^2\gamma \\[2mm] m\,c\,\tan^2\gamma & J_G + m\,c^2\tan^2\gamma \end{bmatrix}\begin{bmatrix} \dot{\sigma} \\ \dot{\omega} \end{bmatrix}$$
$$+ \begin{bmatrix} m\dfrac{\tan\gamma}{\cos^2\gamma}\left(\sigma + c\,\omega - \hat{v}^*\sin\gamma\right)\dot{\gamma} + m\left(\dfrac{\hat{v}^*}{\cos\gamma} - c\,\omega\tan\gamma\right)\omega \\[3mm] m\,c\dfrac{\tan\gamma}{\cos^2\gamma}\left(\sigma + c\,\omega - \hat{v}^*\sin\gamma\right)\dot{\gamma} + m\,c\,\sigma\,\omega\tan\gamma \end{bmatrix}$$
$$= \begin{bmatrix} F_R(\alpha_R) + \dfrac{F_F(\alpha_F)}{\cos\gamma} \\[3mm] -d\,F_R(\alpha_R) + \dfrac{c\,F_F(\alpha_F)}{\cos\gamma} \end{bmatrix} \tag{36}$$

where the dependency of the tire forces on the slip angles α_R and α_F are spelled out again, cf. (28). These can be determined by using the components of the velocities in (34):

$$\tan \alpha_R = -\frac{(\sigma - d\,\omega)\cos\gamma}{\hat{v}^* - (\sigma + c\,\omega)\sin\gamma},$$
$$\tan(\alpha_F - \gamma) = -\frac{(\sigma + c\,\omega)\cos\gamma}{\hat{v}^* - (\sigma + c\,\omega)\sin\gamma}, \tag{37}$$

where the second formula can be simplified to the more practical form

$$\tan \alpha_F = \tan\gamma - \frac{\sigma + c\,\omega}{\hat{v}^*\cos\gamma}, \tag{38}$$

that can be used in (41).

The equations of motion of the front wheel drive automobile are given by the 5 first order Eqs. (32), (36), (37). Again, considering small steering angles and small slip angles, which also yields $\hat{v}^* \approx v^*$, (36) simplifies to (3) and (37) simplifies to (2). That is, the front wheel drive model also simplifies to the traditional model under the small angle assumption. Note however that the kinematics of the FWD model is given by (32) (and not by (21)) which result in the radii

$$R_G = \frac{\sqrt{\left(\dfrac{\hat{v}^*}{\cos\gamma^*} - (\sigma^* + c\,\omega^*)\tan\gamma^*\right)^2 + (\sigma^*)^2}}{\omega^*}, \tag{39}$$
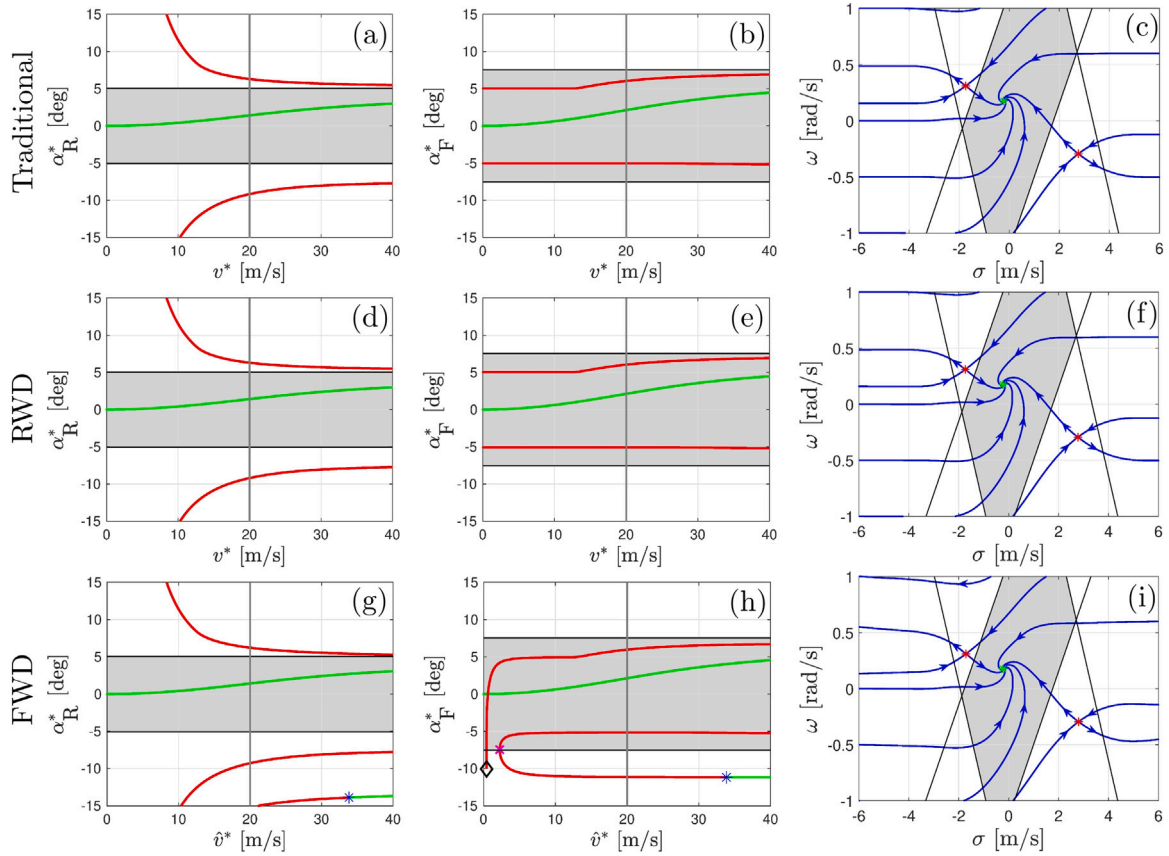
and

$$R_R = \frac{\sqrt{\left(\dfrac{\hat{v}^*}{\cos\gamma^*} - (\sigma^* + c\,\omega^*)\tan\gamma^*\right)^2 + (\sigma^* - d\,\omega^*)^2}}{\omega^*}, \tag{40}$$

in case of steady state cornering (cf. (7) and (8)).

4. Nonlinear analysis

In this section we analyze the nonlinear dynamics of the models developed above by utilizing numerical continuation. Namely, we study the traditional nonlinear model (2), (3) described in Section 2, the rear wheel drive model (28), (29), (30) and the front wheel drive model

Fig. 4. Bifurcation diagrams (a,b,d,e,g,h) and phase portraits (c,f,i) for three models with steering angle $\gamma^* = 2\,[\text{deg}]$. Stable and unstable steady states are denoted by green and red colors, respectively. Gray shading indicates the domains where the slip angles are smaller than α_{pk}. In the bifurcation diagrams the blue stars indicate Hopf bifurcations, magenta crosses denote fold bifurcations, and black diamonds mark singularities. (For interpretation of the references to color in this figure legend, the reader is referred to the web version of this article.)

(36), (37), (38) developed in Section 3. Note that for the analysis below the kinematic Eqs. (1), (21), and (32) can be dropped.

We utilize the numerical continuation software DDE-Biftool (Sieber et al., 2014) in order to find steady states while fixing the steering angle γ^* and changing the velocity v^* (for the traditional and RWD models) or the velocity $\hat{v}^*$ (for the FWD model). The steady state equations were shown in (5) for the traditional model but we do not spell out the formulae for the RWD and FWD models for simplicity. Apart from finding the steady state lateral velocity σ^*, steady state yaw rate ω^*, and steady state slip angles α_R^*, α_F^*, DDE-biftool also evaluates stability by linearizing the equations around the steady state. These were calculated analytically in (16) for the traditional model but are not spelled out for the RWD and FWD models due to algebraic complexity.

Fig. 4 shows the numerical continuation results when setting the steering angle to $\gamma^* = 2\,[\text{deg}]$. The top, middle, and bottom rows correspond to the traditional, RWD, and FWD models, respectively. Panels (a) and (b) display the bifurcation diagrams for the traditional model. In particular, the steady state slip angles α_R^* and α_F^* are plotted as function of the longitudinal velocity v^*. Stable and unstable states are shown by green and red curves, respectively. Gray shading highlights the domain where the slip angles are below the limit α_{pk}, i.e., $|\alpha_R| \leq \alpha_{\text{pk}}$ and $|\alpha_F| \leq \alpha_{\text{pk}}$; cf. (2) and Fig. 1(b).

The stable steady state stays within this region and slip angles increase with the speed. This state correspond to negotiating a curve without saturating the tires and we refer to this as regular turning in the rest of the paper. There are also two unstable states which move closer to the stable state as the speed increases. The upper unstable steady state corresponds to the motion where the rear tire is saturated and the vehicle is taking a sharper turn compared to the regular turning motion, so we refer to this as sharp turning in the rest of the paper. On the other

hand, the lower unstable steady state corresponds to drifting, i.e., the vehicle is turning (with saturated rear tire) to the opposite direction than the steering wheel's direction would suggest.

The phase portrait in Fig. 4(c) is drawn for $v^* = 20\,[\text{m/s}]$; cf. solid vertical line in panels (a) and (b). Stable and unstable steady states are indicated by green and red points, respectively, while trajectories for different initial conditions are shown by blue curves. The gray domain indicates where $|\alpha_R| \leq \alpha_{\text{pk}}$ and $|\alpha_F| \leq \alpha_{\text{pk}}$ and it is obtained via (2). This provides an estimate for the region of attraction for stable steady state, which is given accurately by the stable manifolds of the unstable steady states. When choosing initial condition outside of these manifolds the vehicle spins away from the stable motion. This is often utilized by law enforcement officers to stop a fleeing vehicle: the pursuing vehicle shall hit the rear of the fleeing vehicle hard enough to make it spin.

Fig. 4(d,e) show the bifurcation diagrams for the RWD model. The corresponding phase portrait for $v^* = 20\,[\text{m/s}]$ is shown in Fig. 4(f) where the gray regions are obtained from $|\alpha_R| \leq \alpha_{\text{pk}}$ and $|\alpha_F| \leq \alpha_{\text{pk}}$ using (29), (30). When comparing the results with the traditional model, a high level of similarity can be noticed. That is, for small steering angles the traditional and the RWD models are essentially equivalent in the speed regime investigated.

For the FWD model the bifurcation diagrams and the phase portrait are displayed in Fig. 4(g,h) and (i), respectively, and (37), (38) is used to obtain the gray shaded domain in panel (i) from $|\alpha_R| \leq \alpha_{\text{pk}}$ and $|\alpha_F| \leq \alpha_{\text{pk}}$. While the stable branch behaves similar as in the traditional and RWD cases, the unstable branches show qualitative differences. In particular, the upper branch, corresponding to sharp turning, displays a singularity at small speed (indicated by black diamond) while the drifting branch at the bottom folds back (marked by magenta cross) and also gains stability via a Hopf bifurcation (denoted by blue star)
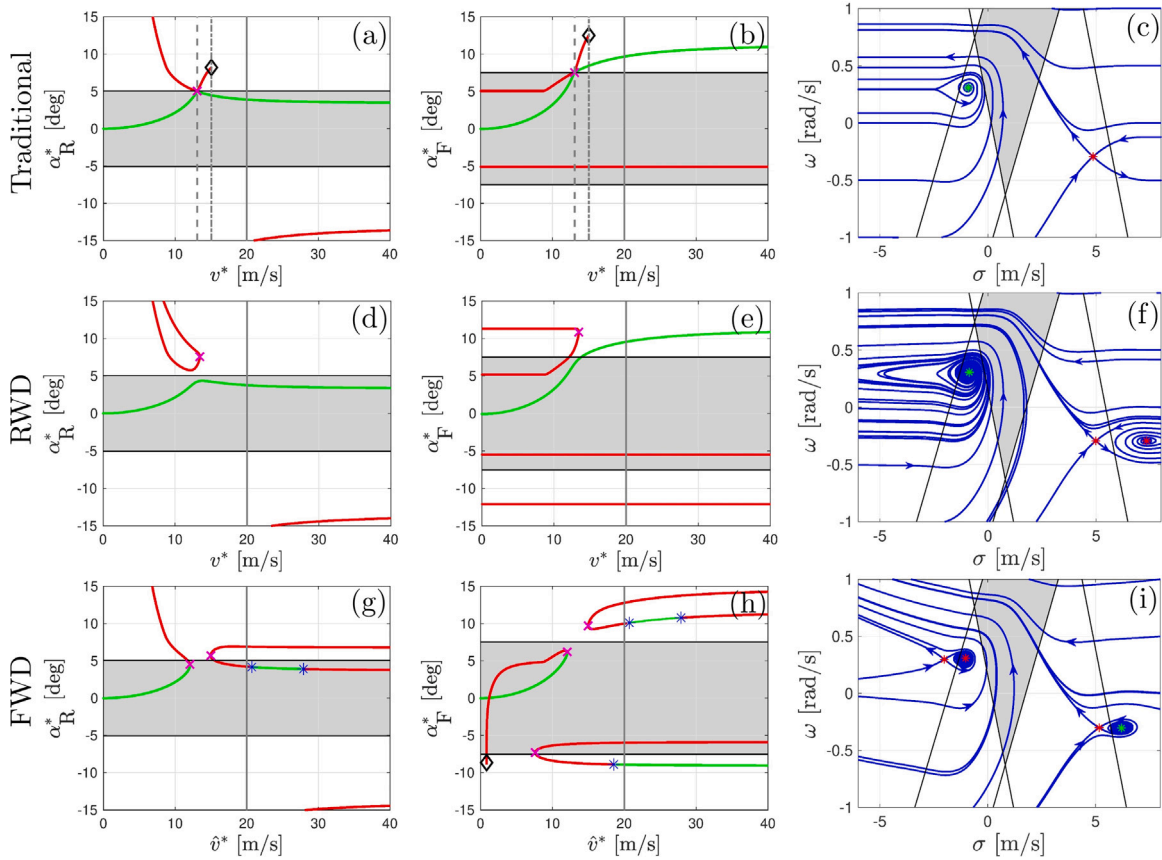
Fig. 5. Bifurcation diagrams (a,b,d,e,g,h) and phase portraits (c,f,i) for three models with steering angle $\gamma^* = 8\,[\mathrm{deg}]$. Stable and unstable steady states are denoted by green and red colors, respectively. Gray shading indicates the domains where the slip angles are smaller than α_{pk}. In the bifurcation diagrams the blue stars indicate Hopf bifurcations, magenta crosses denote fold bifurcations, and black diamonds mark singularities. (For interpretation of the references to color in this figure legend, the reader is referred to the web version of this article.)

for larger speed. Due to the fold, there exist two drifting solutions, one of these is outside of the window in Fig. 4(i). The Hopf bifurcation is subcritical (Guckenheimer and Holmes, 1983; Kuznetsov, 2004) and results in an unstable periodic orbit around the stable steady state. The amplitude of the periodic orbit is very small and this orbit gives the region of attraction of the stable steady state. These qualitative differences, however, only influence the behavior for large slip angles or for small speed. The rest of the diagram still looks akin to that of the traditional model.

We remark that from Fig. 4 one may also infer how the bifurcation diagrams and phase portraits look like in the limit $\gamma^* = 0$. In this case, the stable steady state remains at zero as the speed increases. This corresponds to the rectilinear motion. The unstable steady states appear symmetrically around the stable one and these correspond to special motions where the vehicle turns despite zero steering angle.

Fig. 5 depicts the bifurcation diagrams and phase portraits for steering angle $\gamma^* = 8\,[\mathrm{deg}]$. For the traditional model the bifurcation diagrams (panels (a,b)) show qualitative differences compared to the $\gamma^* = 2\,[\mathrm{deg}]$ case in Fig. 4(a,b). As the speed is increased the stable branch reaches the peak slip angle where it meets with the upper unstable branch of sharp turning via a degenerate fold bifurcation (indicated by magenta cross). The corresponding speed $v^*_{\mathrm{cr},1}$, given by (13), is highlighted by the vertical dashed line. Such critical point only exist due to the "symmetry" of the traditional model which causes both wheels to reach the handling limit at the same speed. However, reminiscences of this bifurcation will show up for the RWD and FWD models as explained below.

As the speed is increased further a stable branch arises for which the rear slip angle stays smaller than the peak value α_{pk} while the front slip angle becomes larger and the front tire saturates. An unstable

branch with both slip angles being larger than the peak value also arises. This ends in a singularity (marked by black diamond) when the speed reaches the critical value $v^*_{\mathrm{cr},2}$, given by (15), that is marked by the vertical dashed–dotted line. For higher speeds only two solutions exists: the stable steady state with saturated front tire and the unstable drifting state with saturated rear tire. These are shown in Fig. 5(c) that highlights that the stable state has a small region of attraction which is not anymore approximated by the gray shaded domain given by $|\alpha_R| \le \alpha_{\mathrm{pk}}$ and $|\alpha_F| \le \alpha_{\mathrm{pk}}$; cf. (2).

The bifurcation diagrams of the RWD model, displayed in Fig. 5(d,e), show some similarities to the those of the traditional model. The biggest change is that the degenerate fold bifurcation is broken, resulting in two separate branches. The stable branch behaves similar to the traditional model while the unstable branch folds back (as marked by the magenta cross). The phase portrait in Fig. 5(f) reveals that there also exist multiple unstable drifting states, one of which is outside of the window in the bifurcation diagram as the slip angles are (unrealistically) large. Again, the shaded region given by $|\alpha_R| \le \alpha_{\mathrm{pk}}$ and $|\alpha_F| \le \alpha_{\mathrm{pk}}$ (cf. (29), (30)) is not related to the region of attraction of the stable steady state.

For the FWD model, as depicted in Fig. 5(g,h), the degenerate fold bifurcation is broken in another way, resulting in two folding branches (see magenta crosses). For lower speed we obtain steady states of stable regular turning and unstable sharp turning (with saturated rear tire). For higher speed we have sharp turning motions with saturated tires that are mostly unstable (see top branches). Even when stability is gained via subcritical Hopf bifurcation (see blue stars) the resulting stable motion has very small region of attraction (given by a small periodic orbit). Similar behavior can be observed for the branches corresponding to drifting (see bottom branches). The phase portrait in
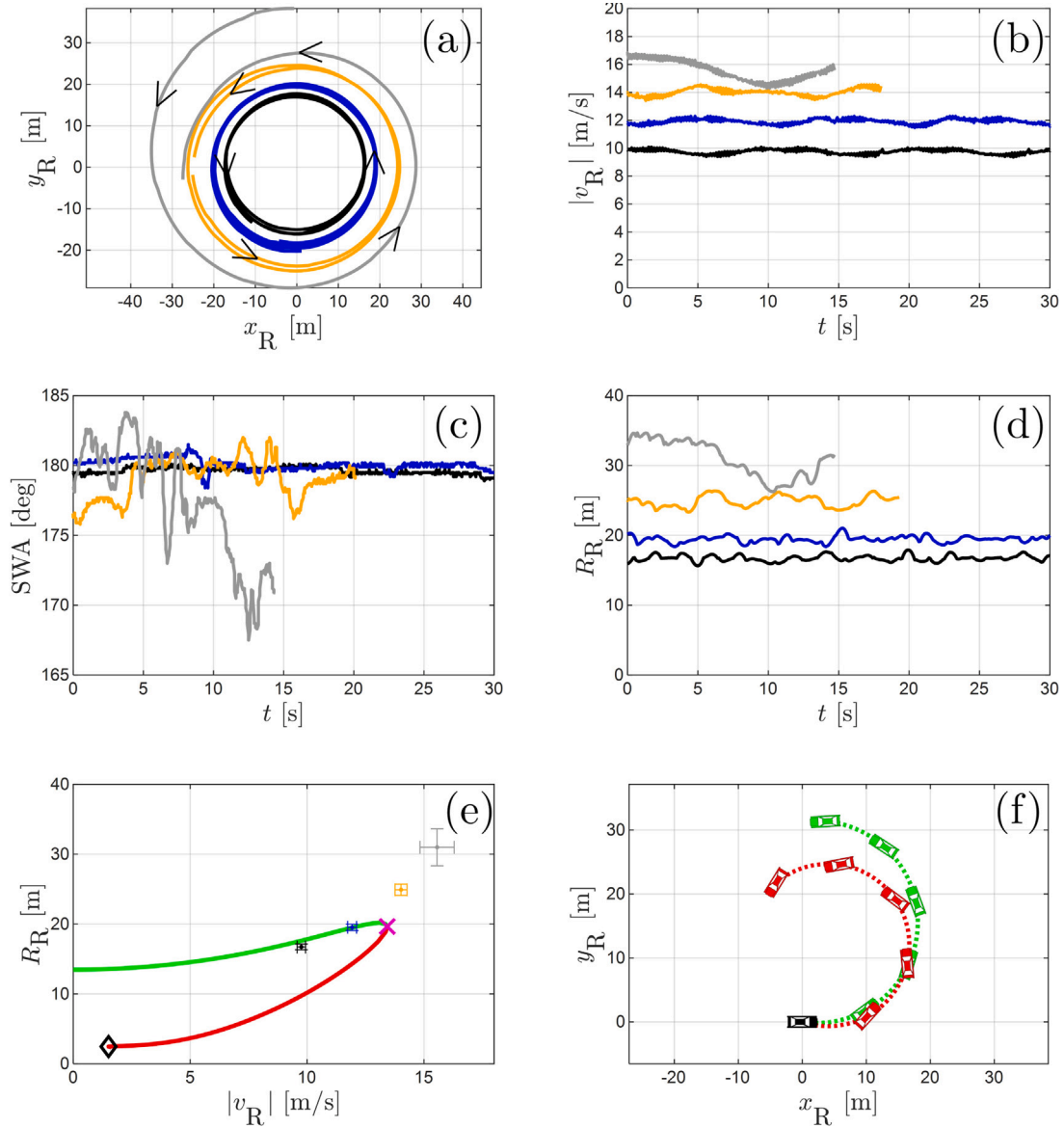
Fig. 6. Experimental results for steady state cornering when the steering wheel angle is set to 180 degrees and the speed is set to 10.0 m/s (black), 12.5 m/s (blue), 15.0 m/s (orange), 17.5 m/s (gray). (a) Trajectories of the rear axle center point R. (b,c,d) Speed of the point R, steering wheel angle, turning radius of the point R as function of time. (e) Turning radius as a function of speed. The colored curves correspond to those on the left side of Fig. 5(g,h). (f) Trajectories of R for regular turning and sharp turning for set speed 12.5 m/s obtained by simulations. (For interpretation of the references to color in this figure legend, the reader is referred to the web version of this article.)

Fig. 5(i) suggests that no stable motion with practically-sized region of attraction exists for large speed, as opposed to what suggested by the gray shaded domain given by $|\alpha_R| \leq \alpha_{pk}$ and $|\alpha_F| \leq \alpha_{pk}$; cf. (37), (38). The most notable phenomenon observed for the FWD model is that there exist a range of speed where neither regular nor fast turning motion happens. This behavior will be confirmed experimentally in Section 5 using an automated vehicle.

To summarize, the bifurcation analysis performed above reveals the similarities and differences between different models. For small steering angles the traditional, RWD, and FWD models show similar behavior (except for small speed) but such statement does not hold for larger steering angles. In the latter case, the traditional model can still provide some guidance, in particular regarding the critical speed, but differentiating the drive type seems critical in understanding the dynamics at large steering angles and speeds. In the next section we show experimental results obtained for a front wheel drive vehicle and compare those to the theoretical results discussed above.

Table 2
Experimental results for steady state cornering with steering wheel angle set to 180 degrees.

Set speed	Measured speed $|v_R|$	SWA	Turning radius R_R
10.0 [m/s]	9.75 ± 0.17 [m/s]	180.02 ± 0.34 [deg]	16.72 ± 0.41 [m]
12.5 [m/s]	11.92 ± 0.19 [m/s]	180.11 ± 0.95 [deg]	19.53 ± 0.45 [m]
15.0 [m/s]	14.02 ± 0.26 [m/s]	178.27 ± 2.37 [deg]	24.91 ± 0.80 [m]
17.5 [m/s]	15.56 ± 0.73 [m/s]	176.13 ± 4.14 [deg]	30.99 ± 2.65 [m]

5. Experimental validation

In this section, we present the results of the steady state cornering experiments and compare to those obtained by bifurcation analysis in the previous section. In particular, we demonstrate that the experimental results match with the theoretical results for a front wheel drive automobile when using the FWD model developed in Section 3.2 that includes the appropriate geometric nonlinearities. We emphasize that

the RWD model developed in Section 3.1 and the traditional model analyzed in Section 2 would give qualitatively different behavior.

A front wheel drive automated KIA Soul with specifications given in Table 1 were used for the experiment. We tune the parameters $m = 1600$ [kg], $J_G = 2000$ [kg m^2], $k = 2 \times 10^6$ [N/m^2], $\mu = \mu_0 = 1.2$ in accordance with our experimental setup, but these do not lead to qualitative changes in the bifurcation diagrams. The driving tests were performed on dry asphalt at the University of Michigan test track called Mcity. The steering angle was held constant by the human operator while the speed was held constant by the controller. GPS data was collected together with vehicle data including the steering angle and the wheel based velocity. The GPS antenna was mounted above the center of the rear axle (see point R in Fig. 1) and below we display the position and speed of this point.

The experimental results are shown in Fig. 6 where panel (a) depicts the traces of the rear center point R for four different set speed values: 10.0 [m/s] (black), 12.5 [m/s] (blue), 15.0 [m/s] (orange), 17.5 [m/s] (gray). The steering wheel angle is set to 180 degrees which corresponds to $\gamma^* \approx 11$ degrees at the wheel (given the steering ratio 15.7). Corresponding to the constant steering angle the vehicle is moving on a circular path and the size of this circle increases with the speed. Steady state cornering cannot be maintained for a full circle for the largest set speed as shown by the gray trajectory. We remark that in reality the paths observed during the experiments for different set speed values were not concentric but we shifted them to increase the readability of the figure.

Fig. 6(b) displays the corresponding speed as a function of time; see Table 2 for the corresponding mean and standard deviation values. One may notice that the higher the set speed is the larger the speed errors are. This is due to the fact that the longitudinal control was achieved by a proportional controller that did not compensate for the resistance arising from steering, i.e., the force component $F_F \sin \gamma^* \approx 0.2 F_F$; see Fig. 1(a). The steering wheel angle SWA and the turning radius R_R are shown in Fig. 6(c) and (d), respectively, as function of time, while the corresponding mean and standard deviation values are given in Table 2. Again, observe that the errors of the steering wheel angle and the turning radius increase with the set speed and for set speed 17.5 [m/s] the steady state cannot be sustained. We remark that the turning radius we obtained by locally fitting arcs to the trajectories using a window size of 19 points.

Fig. 6(e) summarizes the experimental results by displaying the turning radius as function of the measured speed. The dots mark the mean values while the error bars indicate the standard deviations for each experiment. These results are compared with those obtained via bifurcation analysis; cf. Fig. 5(g,h). In particular, the radius R_R is calculated using (40) with $\gamma^* = 11$ [deg], while we also use $|v_R| = \omega^* R_R$; cf. (34), (40). There is good agreement between the theoretically obtained stable branch (green) and the experimental measurements (black, blue, orange, gray squares). In particular, we emphasize the qualitative agreement that no steady state exists above a critical speed; cf. the magenta cross denoting the fold bifurcation and the data point for the highest speed (where no steady state was found). We remark that such qualitative agreement holds for an extended set of vehicle parameters, that is, this behavior is a robust feature of the FWD model developed in this paper.

While the measurement data fit the stable branch in Fig. 6(e), the unstable branch also reveals some interesting dynamics. In particular, observe that the unstable steady state indeed corresponds to sharp turning (smaller radius than the stable steady state cornering) with saturated rear tire; cf. Fig. 5(g,h). The corresponding trajectories of the rear axle center point R, obtained via numerical simulations, are depicted in Fig. 6(f) for set speed 12.5 [m/s]. When linearizing the FWD model (36), (37), (38) around these steady states one obtains a model similar to (16). This way one can show that the sharp turning motion is controllable (at least at the linear level) by modulating the steering angle. This suggests that, with the appropriate controllers, FWD automated automobiles may execute sharp turns, and thus, achieve enhanced maneuverability.

6. Conclusion

High fidelity single track models were developed to describe the lateral and yaw motion of automated vehicles. The models differentiate between front wheel drive and rear wheel drive automobiles by incorporating the geometric nonlinearities beside the tire nonlinearities. The steady state cornering behavior was analyzed with the help of numerical bifurcation analysis that allowed us to compare the newly developed models to a traditional nonlinear model which omits geometric nonlinearities. It was demonstrated that for small steering angles the three models were essentially equivalent and they all exhibited three qualitatively different motions: regular turning, sharp turning, and drifting. In the latter two cases the rear tires were saturated. For larger steering angles similar motions appeared but the models exhibited significant differences about how the motions changed as the speed of the vehicle was increased. The front wheel drive model was validated experimentally by using an automated vehicle on a test track. Experiments confirmed the existence of a region where neither regular nor sharp turning motions existed. The potential of exploiting sharp turning and drifting motions to enhance maneuverability of automated vehicles has been highlighted but the corresponding control design was left for future research. Including the effects of combined slip in the models is another important future direction.

Appendix

Here we provide the algebraic formulae for the nonlinear tire characteristics shown in Fig. 1(b). For the brush model (blue curve), assuming parabolic pressure distribution along the tire-ground contact region one may obtain the form

$$F(\alpha) = \begin{cases} \phi_1 \tan\alpha + \phi_2 \tan^2\alpha \, \text{sgn}\,\alpha + \phi_3 \tan^3\alpha, & \text{if} \quad 0 \le |\alpha| < \alpha_{\text{sl}}, \\ \mu F_z \, \text{sgn}\,\alpha, & \text{if} \quad \alpha_{\text{sl}} < |\alpha|, \end{cases}$$

$$(41)$$

with coefficients

$$\phi_1 = 2ka^2,$$
$$\phi_2 = -\frac{(2ka^2)^2}{3\mu_0 F_z}\left(2 - \frac{\mu}{\mu_0}\right),$$
$$\phi_3 = \frac{(2ka^2)^3}{(3\mu_0 F_z)^2}\left(1 - \frac{2\mu}{3\mu_0}\right),$$

$$(42)$$

and sliding limit

$$\alpha_{\text{sl}} = \arctan\left(\frac{3\mu_0 F_z}{2ka^2}\right).$$

$$(43)$$

Here a is the contact patch half-length, k is the distributed lateral stiffness of the tires, F_z is the vertical load on the axles, μ and μ_0 are the friction coefficients between the tires and the road for sliding and sticking, respectively. Notice that k and a only show up as $2ka^2$ in the above formulae. A simplified version of this model with $\mu = \mu_0$ can be found in Fiala (1954)

Using (41), (42) one may derive the location and the value of the peak as

$$\alpha_{\text{pk}} = \arctan\left(\frac{\mu_0 F_z}{2ka^2}\left(1 - \frac{2\mu}{3\mu_0}\right)^{-1}\right),$$
$$F(\alpha_{\text{pk}}) = \mu_0 F_z\left(\frac{4}{3} - \frac{\mu}{\mu_0}\right)\left(1 - \frac{2\mu}{3\mu_0}\right)^{-2}, \tag{44}$$

and the cornering stiffness

$$\frac{\mathrm{d}F}{\mathrm{d}\alpha}(0) = 2ka^2. \tag{45}$$

The green curve in Fig. 1(b) is given by the magic formula

$$F(\alpha) = D\sin\left(\tilde{C}\arctan\left(B(1-E)\tan\alpha + E\arctan\left(B\tan\alpha\right)\right)\right), \tag{46}$$

where the four independent parameters $A, B, \tilde{C}, D$ are typically identified experimentally. One may calculate the lateral force corresponding to complete sliding

$$F(\pi/2) = D\sin(\tilde{C}\pi/2), \tag{47}$$

the location and the value of the peak

$$\alpha_{\text{pk}} = \arctan\left(\frac{\tan\left(f(\tilde{C}, E)\right)}{B}\right),$$
$$F(\alpha_{\text{pk}}) = D, \tag{48}$$

where $f(\tilde{C}, E)$ is the solution of the equation

$$(1 - E)\tan z + Ez + \tan\frac{\pi}{2\tilde{C}} = 0, \tag{49}$$

for z, and the cornering stiffness is given by

$$\frac{\mathrm{d}F}{\mathrm{d}\alpha}(0) = B\tilde{C}D. \tag{50}$$

Then comparing (41), (44), (45) with (47), (48), (50) the parameters of the brush model and the magic formula can be matched.

References

Beregi, S., Takács, D., 2019. Analysis of the tyre–road interaction with a non-smooth delayed contact model. Multibody Syst. Dyn. 45, 185—201.

Berntorp, K., Quirynen, R., Uno, T., Cairano, S.D., 2020. Trajectory tracking for autonomous vehicles on varying road surfaces by friction-adaptive nonlinear model predictive control. Veh. Syst. Dyn. 58 (5).

De Sapio, V., 2017. Advanced Analytical Dynamics: Theory and Applications. Cambridge University Press.

Della Rossa, F., Mastinu, G., Piccardi, C., 2012. Bifurcation analysis of an automobile model negotiating a curve. Veh. Syst. Dyn. 50 (10), 1539–1562.

Erlien, S.M., Fujita, S., Gerdes, J.C., 2013. Safe driving envelopes for shared control of ground vehicles. IFAC Proc. Vol. 46 (21), 831–836.

Ersal, T., Kolmanovsky, I., Masoud, N., Ozay, N., Scruggs, J., Vasudevan, R., Orosz, G., 2020. Connected and automated road vehicles: state of the art and future challenges. Veh. Syst. Dyn. 58 (5), 672–704.

Farroni, F., Russo, M., Russo, R., Terzo, M., Timpone, F., 2013. A combined use of phase plane and handling diagram method to study the influence of tyre and vehicle characteristics on stability. Veh. Syst. Dyn. 51 (8), 1265–1285.

Fiala, E., 1954. Seitenkräfte am rollenden Luftreifen. Zeitschrift Der Vereines Deutscher Ingenieure 96, 973–979.

Gantmacher, F., 1975. Lectures in Analytical Mechanics. MIR Publishers.

Goh, J.Y., Goel, T., Gerdes, J.C., 2020. Toward automated vehicle control beyond the stability limits: drifting along a general path. J. Dyn. Syst. Measur. Control 142 (2), 021004.

Guckenheimer, J., Holmes, P., 1983. Nonlinear Oscillations, Dynamical Systems, and Bifurcations of Vector Fields. Applied Mathematical Sciences, 42, Springer.

Hwan Jeon, J., Cowlagi, R.V., Peters, S.C., Karaman, S., Frazzoli, E., Tsiotras, P., Iagnemma, K., Optimal motion planning with the half-car dynamical model for autonomous high-speed driving, in: American Control Conference, 2013, pp. 188–193.

Kuznetsov, Y.A., 2004. Elements of Applied Bifurcation Theory, third ed. Applied Mathematical Sciences, 112, Springer.

Li, S.E., Chen, H., Li, R., Liu, Z., Wang, Z., Xin, Z., 2020. Predictive lateral control to stabilise highly automated vehicles at tire-road friction limits. Veh. Syst. Dyn. 58 (5).

Liu, J., Jayakumar, P., Stein, J.L., Ersal, T., 2016. A study on model fidelity for model predictive control-based obstacle avoidance in high-speed autonomous ground vehicles. Veh. Syst. Dyn. 54 (11), 1629–1650.

Lu, H., Stépán, G., Lu, J., Takács, D., 2021. The effect of time delay on vehicle stability control. Veh. Syst. Dyn. submitted.

Mi, T., Stépán, G., Takács, D., Chen, N., 2020. Vehicle shimmy modeling with Pacejka's magic formula and the delayed tire model. J. Comput. Nonlinear Dyn. 15 (3), 031005.

Ono, E., Hosoe, S., Tuan, H.D., Doi, S., 1998. Bifurcation in vehicle dynamics and robust front wheel steering control. IEEE Trans. Control Syst. Technol. 6 (3), 412–420.

Pacejka, H., 2005. Tire and Vehicle Dynamics. Elsevier.

Paden, B., Čáp, M., Yong, S.Z., Yershov, D., Frazzoli, E., 2016. A survey of motion planning and control techniques for self-driving urban vehicles. IEEE Trans. Intell. Veh. 1 (1), 33–55.

Popp, K., Schiehlen, W., 2010. Ground Vehicle Dynamics. Springer.

Rajamani, R., 2012. Vehicle Dynamics and Control. Springer.

Riekert, P., Schunck, T.-E., 1940. Zur fahrmechanik des gummibereiften kraftfahrzeugs. Ing.-Arch. 11 (3), 210–224.

Schramm, D., Hiller, M., Bardini, R., 2014. Ground Vehicle Dynamics. Springer.

Sieber, J., Engelborghs, K., Luzyanina, T., Samaey, G., Roose, D., 2014. DDE-BIFTOOL Manual-bifurcation analysis of delay differential equations. ArXiv Preprint ArXiv:1406.7144.

Ulsoy, A.G., Peng, H., Cakmakci, M., 2012. Automotive Control Systems. Cambridge University Press.

Várszegi, B., Takács, D., Orosz, G., 2019. On the nonlinear dynamics of automated vehicles – a nonholonomic approach. Eur. J. Mech. A 74, 371–380.

Velenis, E., Katzourakis, D., Frazzoli, E., Tsiotras, P., Happee, R., 2011. Steady-state drifting stabilization of RWD vehicles. Control Eng. Pract. 19 (11), 1363–1376.

Voser, C., Hindiyeh, R.Y., Gerdes, J.C., 2010. Analysis and control of high sideslip manoeuvres. Veh. Syst. Dyn. 48 (S1), 317–336.

Wurts, J., Stein, J.L., Ersal, T., 2020. Collision imminent steering at high speed using nonlinear model predictive control. IEEE Trans. Control Syst. Technol. 69 (8), 8278–8289.

Zhang, H., Cao, D., Du, H., 2018. Modeling, Dynamics, and Control of Electrified Vehicles. Springer.